Angle-domain common image gathers for anisotropic migration

Biondo Biondi[1]

ABSTRACT

I present a general methodology for computing Angle-Domain Common Image Gathers (ADCIGs) in conjunction with anisotropic wavefield-continuation migration. The method is based on the transformation of the prestack image from the subsurface-offset domain to the angle domain by use of slant stacks. The processing sequence is the same as for the computation of ADCIGs for the isotropic case, though the interpretation of the relationship between the slopes measured in the prestack image and the aperture angles are more complex. I demonstrate that the slopes measured by performing slant stack along the subsurface-offset axis of the prestack image are a good approximation of the phase aperture angles, and that they are exactly equal to the phase aperture angles for flat reflectors in Vertical Transverse Isotropic (VTI) media. In the general case of dipping reflectors, the true aperture angles can be easily computed as a function of the reflector dip and anisotropic slowness at the reflector.

I derive the relationships between phase angles and slopes measured in the prestack image from both a "plane-wave" viewpoint and a "ray" viewpoint. The two derivations are consistent with each other, as demonstrated by the fact that in the special case of flat reflectors they lead to exactly the same expression. The ray-theoretical derivation is based on a novel generalization of kinematic migration to the computation of prestack images as a function of the subsurface offset. This theoretical development leads to the linking of the kinematics in ADCIGs with migration-velocity errors, and thus it enables the use of ADCIGs for velocity estimation.

I apply the proposed method to the computation of ADCIGs from the prestack image obtained by anisotropic migration of a 2-D line extracted from a Gulf of Mexico 3-D data set. The analysis of the error introduced by neglecting the difference between the true phase aperture angle and the angles computed through slant stack shows that these errors are negligible and can be safely ignored in realistic situations. On the contrary, group aperture angles can be quite different from phase aperture angles and thus ignoring the distinction between these two angles can be detrimental to practical applications of ADCIGs.

---

[1]**email:** biondo@sep.stanford.edu

INTRODUCTION

Angle-Domain Common Image Gathers (ADCIGs) have become a common tool for analyzing prestack images obtained by wavefield-continuation migration. They can be used for both updating migration velocity after wavefield-continuation migration (Biondi and Sava, 1999; Clapp and Biondi, 2000), as well as the analysis of amplitudes as a function of aperture angle (Wang et al., 2005).

All the present methods for computing ADCIGs in conjunction with wavefield migration are limited to isotropic migration; this is true for both the methods applied during downward continuation before imaging (Prucha et al., 1999), and the methods applied on the prestack migrated image as a post-processing operator (Sava and Fomel, 2003; Rickett and Sava, 2002; Biondi and Tisserant, 2004). Similarly, the quantitative analysis of the residual moveout measured in ADCIGs caused by migration-velocity errors is also limited to the isotropic case (Biondi and Symes, 2003; Biondi and Tisserant, 2004).

In this paper I generalize the methodologies for computing and analyzing ADCIGs to prestack images obtained by wavefield-continuation anisotropic migration. In a companion paper (Biondi, 2005) I derive the expressions for computing residual moveout in ADCIGs as a function of errors in the anisotropic parameters used for migration. This work is practically motivated by two current trends in the seismic exploration industry: 1) data are recorded with increasingly longer offsets, widening the range of propagation angles and thus making the inclusion of anisotropic effects crucial to the complete focusing of reflections, 2) anisotropic prestack depth migration is increasingly being used in areas, like near or under salt bodies, where the image quality, and consequently the velocity estimation process, could benefit from the use of wavefield-continuation migration (Bear et al., 2003; Sarkar and Tsvankin, 2004).

The main conceptual differences between isotropic ADCIGs and anisotropic ADCIGs are related to the fact that in anisotropic wave propagation the phase angles and velocities are different from the group angles and velocities (Tsvankin, 2001). Therefore, I will first address the question of which aperture angles we are measuring in the ADCIGs. I demonstrate that the transformation to angle domain maps the reflection into the phase-angle domain. Strictly speaking, this mapping is exact only for events normal to the isotropic axis of symmetry (e.g. flat events for Vertical Transverse Isotropic (VTI) media), because the presence of dips biases the estimates. This bias is caused by the difference in propagation velocity between the incident and the reflected waves, and thus for VTI media it is small unless the anisotropy is strong and the dips steep. The real-data example shown in this paper indicates that, for realistic values of anisotropy, the errors caused by the geological dips are small and can be neglected. This approximation greatly simplifies the computation of ADCIGs and thus makes their application more attractive. When the accuracy of this approximation is not sufficient, the true aperture angles can be easily computed from the measured slopes in the prestack image by iteratively solving a system of two non-linear equations, which usually converge to the solution in only few iterations.

The methodology developed in this paper is limited to the the imaging of acoustic data and thus is limited to the acoustic approximation of elastic anisotropic wave propagation. Further-

more, the numerical examples are limited to VTI media defined by their vertical velocity and two of the three Thomsen parameters: ϵ, δ, and η. However, the basic concepts have a general validity and the generalization to more general anisotropic media, such as Tilted Transverse Isotropic (TTI) media should be fairly straightforward, though outside the scope of this paper.

PHASE AND GROUP ANGLES AND VELOCITIES

In anisotropic wave propagation the phase angles and velocities are different from the group angles and velocities. In this section I briefly review the concepts of phase and group angles and velocities and the relationships between these physical quantities. I also define the particular approximation to a VTI medium that I use in the numerical examples.

The transformation from phase velocity $\widetilde{V}$ to group velocity V is conventionally defined as the following (Tsvankin, 2001):

$$V = \sqrt{\widetilde{V}^2 + \left(\frac{d\widetilde{V}}{d\widetilde{\theta}}\right)}, \tag{1}$$

where $\widetilde{\theta}$ is the phase propagation angle. The associated transformation from phase angles to group angles θ is defined as:

$$\tan\theta = \frac{\tan\widetilde{\theta} + \frac{1}{V}\frac{d\widetilde{V}}{d\theta}}{1 - \frac{1}{V}\frac{d\widetilde{V}}{d\theta}\tan\widetilde{\theta}}. \tag{2}$$

Notice that throughout this paper I use the tilde symbol to distinguish between phase quantities (with a tilde) and group quantities (without a tilde).

Dellinger and Muir (1985) propose, and heuristically motivate, the following symmetric relations for the inverse transforms:

$$\widetilde{S} = \sqrt{S^2 + \left(\frac{dS}{d\theta}\right)}, \tag{3}$$

where $\widetilde{S}$ and S are respectively the phase slowness and the group slowness, and

$$\tan\widetilde{\theta} = \frac{\tan\theta + \frac{1}{S}\frac{dS}{d\theta}}{1 - \frac{1}{S}\frac{dS}{d\theta}\tan\theta}. \tag{4}$$

I use the heuristic relation in equation 4 to derive some of the analytical results presented in this paper. Furthermore, I use all the above relationships to compute the kinematic numerical results presented in this paper.

The numerical results, though not the analytical results, are also dependent on the choice of a specific approximation of the anisotropic phase-velocity function. I used the following

VTI approximation for the phase velocity:

$$\widetilde{V}_{\text{VTI}}^2(\theta) = \frac{V_V{}^2\cos^2\theta + V_H{}^2\sin^2\theta + \sqrt{\left(V_V{}^2\cos^2\theta + V_H{}^2\sin^2\theta\right)^2 + V_V{}^2\left(V_N{}^2 - V_H{}^2\right)\sin^2 2\theta}}{2},$$

(5)

where V_V, V_H, V_N, are respectively the vertical velocity, the horizontal velocity and the NMO velocity. Following Fowler (2003), the corresponding approximation for the group velocity is the following:

$$S_{\text{VTI}}^2(\theta) = \frac{S_V{}^2\cos^2\theta + S_H{}^2\sin^2\theta + \sqrt{\left(S_V{}^2\cos^2\theta + S_H{}^2\sin^2\theta\right)^2 + S_V{}^2\left(S_N{}^2 - S_H{}^2\right)\sin^2 2\theta}}{2},$$

(6)

where S_V, S_H, S_N, are respectively the vertical slowness, the horizontal slowness and the NMO slowness.

The numerical results obtained by modeling and migrating synthetic seismic data and by migrating the real data were obtained by source-receiver depth continuation (upward for modeling and downward for migration) using the following dispersion relation:

$$k_z = \frac{\omega}{V_V}\sqrt{\frac{\omega^2 - V_H{}^2 k_x^2}{\omega^2 + \left(V_N{}^2 - V_H{}^2\right)k_x^2}},$$

(7)

where ω is the temporal frequency, and k_x and k_z are respectively the horizontal and vertical wavenumbers. The dispersion relation shown in equation 7 corresponds to the velocity and slowness functions in equations 5 and 6 (Fowler, 2003).

ANGLE GATHERS BY ANISOTROPIC DOWNWARD-CONTINUATION MIGRATION

In this section I develop the theory for anisotropic ADCIGs from the "plane-wave" viewpoint. I assume that in the proximity of the reflection point the source wavefield and the receiver wavefield are plane waves and I derive the relationships between the propagation angles of these plane waves and the slopes computed in the prestack image. This assumption is not restrictive because the source and receiver wavefields can always be considered as the superposition of plane waves.

In anisotropic media, when the reflector is dipping with respect to the normal to the isotropic axis of symmetry (horizontal direction for VTI) the incident and reflected aperture angles differ. This difference is caused by the fact that, although the phase slowness is function of the propagation angle, Snell law requires that the components parallel to the reflector of the incident and reflected slowness vectors must match at the interface. However, we can still define an "average" aperture angle $\widetilde{\gamma}$ and "average" dip angle $\widetilde{\alpha}_x$ using the following relationships:

$$\widetilde{\gamma} = \frac{\widetilde{\beta}_r - \widetilde{\beta}_s}{2}, \quad \text{and} \quad \widetilde{\alpha}_x = \frac{\widetilde{\beta}_s + \widetilde{\beta}_r}{2},$$

(8)
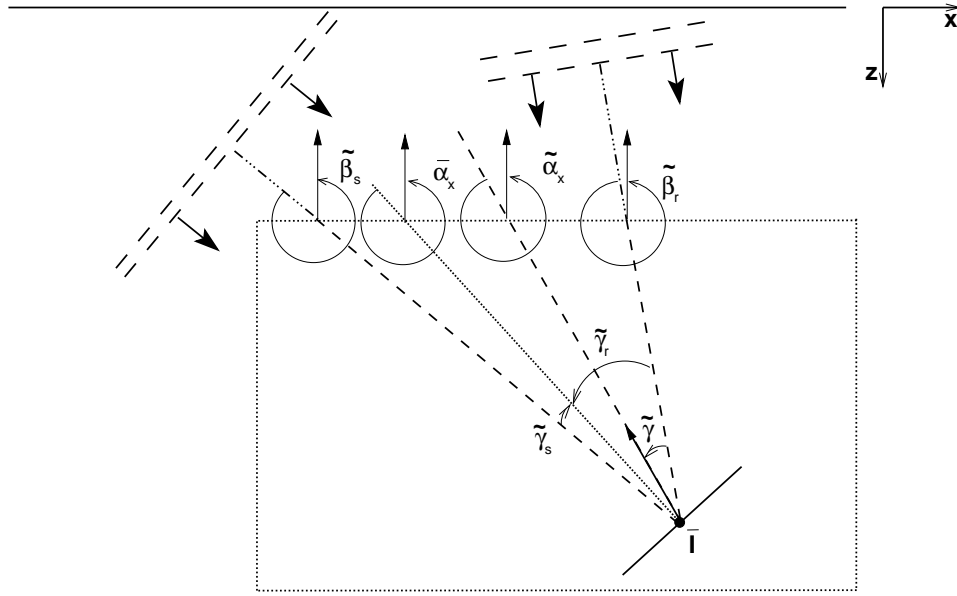
Figure 1: Sketch representing the reflection of a plane wave from a planar reflector in an anisotropic medium. The angles marked in the figure are all phase angles. They are defined as follows: $\widetilde{\beta}_s$ and $\widetilde{\beta}_r$ are the propagation angles of the incident and reflected plane waves, $\widetilde{\gamma}_s$ and $\widetilde{\gamma}_r$ are the true aperture angles for the the incident and reflected plane waves, $\overline{\alpha}_x$ is the true geological dip angle, $\widetilde{\gamma}$ are $\widetilde{\alpha}_x$ the average aperture angle and the average dip angle. biondo1-cig-aniso-v3 [NR]

where the $\widetilde{\beta}_s$ and $\widetilde{\beta}_r$ are the phase angles of the incident and reflected plane waves, respectively.

Figure 1 shows the geometric interpretation of these angles. Notice that the average dip angle $\widetilde{\alpha}_x$ is different from the true geological dip angle $\overline{\alpha}_x$, and that the average aperture angle $\widetilde{\gamma}$ is obviously different from the true aperture angles $\widetilde{\gamma}_s$ and $\widetilde{\gamma}_r$. However, these five angles are related and, if needed, the true angles can be derived from the average angles, as shown in Appendix A.

Prestack images defined in the subsurface-offset (h_ξ) domain are transformed into the angle domain by applying slant stacks. The transformation axis is thus the physical dip of the image along the subsurface offset; that is, $\partial z_\xi / \partial h_\xi$. The dip angles can be similarly related to the midpoint dips in the image; that is, $\partial z_\xi / \partial m_\xi$. Following the derivation of acoustic isotropic ADCIGs by Sava and Fomel (2003) and of converted-waves ADCIGs by Rosales and Rickett (2001), we can write the following relationships between the propagation angles

and the derivative measured from the wavefield:

$$\frac{\partial t}{\partial z_\xi}\bigg|_{(m_\xi=\overline{m}_\xi,\, h_\xi=\overline{h}_\xi)} = \widetilde{S}_s\cos(\widetilde{\alpha}_x-\widetilde{\gamma})-\widetilde{S}_r\cos(\widetilde{\alpha}_x+\widetilde{\gamma}), \tag{9}$$

$$\frac{\partial t}{\partial m_\xi}\bigg|_{(z_\xi=\overline{z}_\xi,\, h_\xi=\overline{h}_\xi)} = \widetilde{S}_s\sin(\widetilde{\alpha}_x-\widetilde{\gamma})+\widetilde{S}_r\sin(\widetilde{\alpha}_x+\widetilde{\gamma}), \tag{10}$$

$$\frac{\partial t}{\partial h_\xi}\bigg|_{(z_\xi=\overline{z}_\xi,\, m_\xi=\overline{m}_\xi)} = \widetilde{S}_s\sin(\widetilde{\alpha}_x-\widetilde{\gamma})-\widetilde{S}_r\sin(\widetilde{\alpha}_x+\widetilde{\gamma}), \tag{11}$$

where $\widetilde{S}_s$ and $\widetilde{S}_r$ are the phase slownesses for the source and receiver wavefields, respectively. We obtain the expression for the offset dip by taking the ratio of equation 11 with equation 9, and similarly for the midpoint dips by taking the ratio of equation 10 with equation 9, and after some algebraic manipulations, we obtain the following expressions:

$$\frac{\partial z_\xi}{\partial h_\xi}\bigg|_{(m_\xi=\overline{m}_\xi)} = \frac{\tan\widetilde{\gamma}+\frac{\widetilde{S}_r-\widetilde{S}_s}{\widetilde{S}_r+\widetilde{S}_s}\tan\widetilde{\alpha}_x}{1-\frac{\widetilde{S}_r-\widetilde{S}_s}{\widetilde{S}_r+\widetilde{S}_s}\tan\widetilde{\alpha}_x\tan\widetilde{\gamma}}, \tag{12}$$

$$\frac{\partial z_\xi}{\partial m_\xi}\bigg|_{(h_\xi=\overline{h}_\xi)} = \frac{\tan\widetilde{\alpha}_x+\frac{\widetilde{S}_r-\widetilde{S}_s}{\widetilde{S}_r+\widetilde{S}_s}\tan\widetilde{\gamma}}{1-\frac{\widetilde{S}_r-\widetilde{S}_s}{\widetilde{S}_r+\widetilde{S}_s}\tan\widetilde{\gamma}\tan\widetilde{\alpha}_x}. \tag{13}$$

In contrast with the equivalent relationships valid for isotropic media, these relationships depend on both the aperture angle $\widetilde{\gamma}$ and the dip angle $\widetilde{\alpha}_x$. The expression for the offset dip (equation 9) simplifies into the known relationship valid in isotropic media when either the difference between the phase slownesses is zero, or the dip angle $\widetilde{\alpha}_x$ is zero. In VTI media this happens for flat geological dips. In a general TTI medium this condition is fulfilled when the geological dip is normal to the axis of symmetry.

Solving for $\tan\widetilde{\gamma}$ and $\tan\widetilde{\alpha}_x$ we obtain the following:

$$\tan\widetilde{\gamma} = \frac{\frac{\partial z_\xi}{\partial h_\xi}-\Delta_{\widetilde{S}}\tan\widetilde{\alpha}_x}{1+\frac{\partial z_\xi}{\partial h_\xi}\Delta_{\widetilde{S}}\tan\widetilde{\alpha}_x}, \tag{14}$$

$$\tan\widetilde{\alpha}_x = \frac{\frac{\partial z_\xi}{\partial m_\xi}-\Delta_{\widetilde{S}}\tan\widetilde{\gamma}}{1+\frac{\partial z_\xi}{\partial m_\xi}\Delta_{\widetilde{S}}\tan\widetilde{\gamma}}, \tag{15}$$

where for convenience I substituted the symbol $\Delta_{\widetilde{S}}$ for the "normalized slowness difference" $(\widetilde{S}_r-\widetilde{S}_s)/(\widetilde{S}_r+\widetilde{S}_s)$.

Substituting equation 15 in equation 14, and equation 14 into equation 15, we get the following two quadratic expressions that can be solved to estimate the angles as a function of the dips measured from the image:

$$\left[\frac{\partial z_\xi}{\partial m_\xi}\Delta_{\widetilde{S}}-\frac{\partial z_\xi}{\partial h_\xi}\Delta_{\widetilde{S}}^2\right]\tan^2\widetilde{\gamma}+\left[1-\Delta_{\widetilde{S}}^2\right]\tan\widetilde{\gamma}+\frac{\partial z_\xi}{\partial m_\xi}\Delta_{\widetilde{S}}-\frac{\partial z_\xi}{\partial h_\xi} = 0, \tag{16}$$

$$\left[\frac{\partial z_\xi}{\partial h_\xi}\Delta_{\widetilde{S}}-\frac{\partial z_\xi}{\partial m_\xi}\Delta_{\widetilde{S}}^2\right]\tan^2\widetilde{\alpha}_x+\left[1-\Delta_{\widetilde{S}}^2\right]\tan\widetilde{\alpha}_x+\frac{\partial z_\xi}{\partial h_\xi}\Delta_{\widetilde{S}}-\frac{\partial z_\xi}{\partial m_\xi} = 0. \tag{17}$$

These are two independent quadratic equations in $\tan \widetilde{\gamma}$ and $\tan \widetilde{\alpha}_x$ that can be solved independently. If the "normalized slowness difference" $\Delta_{\widetilde{s}}$ between the slowness along the propagation directions of the source and receiver wavefields are known, we can directly compute $\widetilde{\gamma}$ and $\widetilde{\alpha}_x$, and then the true $\widetilde{\beta}_s$ and $\widetilde{\beta}_r$. One important case in this category is when we image converted waves.

For anisotropic velocities, the slownesses depend on the propagation angles, and thus the normalized difference depends on the unknown $\widetilde{\gamma}$ and $\widetilde{\alpha}_x$. In practice, these equations can be solved by a simple iterative process that starts by assuming the "normalized difference" to be equal to zero. In all numerical test I conducted this iterative process converges to the correct solution in only a few iterations, and thus is not computationally demanding.

If the anisotropic slowness function were spatially homogeneous, equations 16 and 17 could be solved iteratively in the Fourier domain, and the transformation to the average angles $\widetilde{\gamma}$ and $\widetilde{\alpha}_x$ could be computed exactly without the need of estimating the apparent reflector dip in the space domain. When the anisotropic parameters are a function of the spatial variables; that is, in the majority of the real situations, the solution of equations 16 and 17 requires the estimation of the local reflector dip in the space domain. If necessary, the reflectors' dip can be either extracted from the interpretation of the horizons of interest, or can be automatically estimated from the image by applying one of the several methods that have been presented in the literature (see for example Fomel (2002)). In practice, the estimation of the reflector dip is seldom necessary. The numerical and real-data examples shown below indicate that for practical values of the anisotropy parameters the dependency of the estimate from the dip angles can be safely ignored for small dips, and it is unlikely to constitute a problem for steep dips.

KINEMATIC ANALYSIS OF ADCIGS BY INTEGRAL MIGRATION

The analysis shown in the previous section provides the fundamental equations to relate the offset and midpoint dips measured from prestack images to the phase angles at the reflection point. However, the previous analysis is not directly applicable to the analysis of the kinematic properties of events in the ADCIGs because it is based on plane waves. An important application of ADCIGs is the measurements of residual moveout along the aperture angle (i.e. departure from flatness) caused by velocity errors. To achieve this goal we must relate traveltime errors accumulated during the propagation in the overburden to movements of the migrated events in the ADCIG. This task is easier in the ray domain than in the plane-wave domain because traveltime errors are naturally evaluated along rays, which are related to group velocity and angles. To overcome this obstacle toward the use of ADCIGs for velocity estimation, in this section I introduce an integral formulation of the methodology to compute angle gathers that enables a simple link between ADCIGs and kinematics. The following analysis has also the theoretical value of being independent from the migration method applied to compute the prestack images (integral method or wavefield-continuation method) and thus of providing a conceptual link between the angle gathers obtained using different migration methods.

My analysis is based on the conceptual generalization of integral (Kirchhoff) migration to
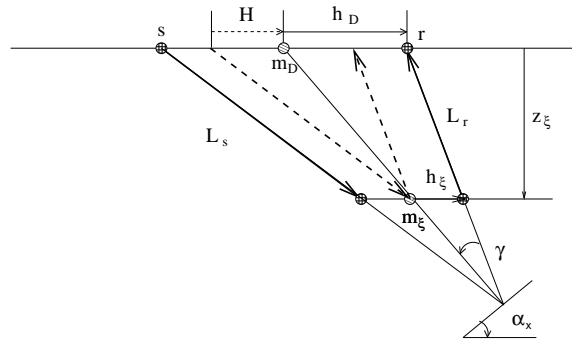
Figure 2: Geometry used for evaluating the impulse response of the generalized integral migration. biondo1-imp-resp [NR]

the computation of sub-surface offset gathers. Integral migration is defined by the summation surfaces over which the data are integrated to compute the image at every point in the image space. The shapes of these summation surfaces are usually computed as the sum of the time delays from the image point (z_ξ, m_ξ) in the subsurface to the source and receiver locations at the surface. The basic idea underlying the generalization I introduce in this paper, is that we can compute the summation surfaces by evaluating the time delays starting not from the same point in the subsurface for both the source and receiver rays, but starting from two points horizontally shifted by $\pm h_\xi$ with respect to the image point. The summation of data along these surfaces produces a prestack image as a function of the subsurface offset that is kinematically equivalent to the image created by wavefield-continuation migrations such as source-receiver downward continuation, or shot-profile migration in conjunction to the generalized imaging condition discussed by Rickett and Sava (2002). Therefore, the kinematic analysis that follows, and its conclusions, are independent from the migration method applied to compute the prestack images. An interesting observation is that the ADCIGs computed using this generalization of integral migration should be immune from the artifacts that affect angle gathers computed by conventional integral migration and discussed by Stolk and Symes (2003).

Generalized migration impulse response in parametric form

Integral migration can be conceptually performed by spreading the data along spreading surfaces as well as by summing data along the summation surfaces discussed above. The spreading surfaces are duals of the summation surfaces and represent the impulse response of the migration operator. In homogeneous anisotropic medium the shape of the impulse responses of the generalized integral migration can be easily evaluated analytically as a function of the subsurface offset h_ξ, in addition to the usual image depth z_ξ and midpoint m_ξ. Figure 2 illustrates the geometry used to evaluate this impulse response. Notice that the angles in this figure (α_x and γ) are missing a tilde because they are group angles, and not phase angles as in the previous section. In an isotropic medium these angles are the dip and aperture angles, but in an anisotropic medium these angles are not easily related to the geological dip and the reflection aperture angles. They can be thought of as convenient parameters to evaluate the impulse response.

   Simple trigonometry applied to Figure 2 allows us to express the impulse response in parametric form, as a function of α_x and γ. If we migrate an impulse recorded at time t_D, midpoint

m_D and surface offset h_D, the migration impulse response can be expressed as follows:

$$z_\xi = L(\alpha_x, \gamma) \frac{\cos^2 \alpha_x - \sin^2 \gamma}{\cos \alpha_x \cos \gamma}, \tag{18}$$

$$m_\xi = m_D - L(\alpha_x, \gamma) \frac{\sin \alpha_x}{\cos \gamma}, \tag{19}$$

$$h_\xi = h_D - H = h_D - L(\alpha_x, \gamma) \frac{\sin \gamma}{\cos \alpha_x}, \tag{20}$$

with

$$L(\alpha_x, \gamma) = \frac{L_s + L_r}{2}. \tag{21}$$

In a isotropic medium the half path-length L would be simply given by $t_D/2S$, but in an anisotropic medium it is function of the angles. Its two components L_s and L_r can be calculated by solving the following system of linear equations:

$$t_D = S_s L_s + S_r L_r, \tag{22}$$

$$z_s - z_r = L_s \cos(\alpha_x - \gamma) - L_r \cos(\alpha_x + \gamma) = 0. \tag{23}$$

Equation 22 constraints the total traveltime to be equal to the impulse time, and equations 23 constraints the depth of the end point of the two rays (z_s and z_r) to be equal, since the subsurface offset is assumed to be horizontal. The solution of this system of equation yields the following for the half path-length:

$$L(\alpha_x, \gamma) = \frac{L_s + L_r}{2} = \frac{t_D}{(S_r + S_s) + (S_r - S_s) \tan \alpha_x \tan \gamma}. \tag{24}$$

The combination of equation 24 and equations 18–20 enables the evaluation of the generalized migration impulse response in a arbitrary homogeneous anisotropic medium.

Figure 3 shows a 3-D rendering of the impulse response computed using the previous equations for an impulse with $t_D = .9$ seconds, $m_D = 0$ kilometers, and $h_D = .4$ kilometers, and vertical slowness $S_V = 1$ s/km. The anisotropic parameters correspond to the Taylor Sand as described by Tsvankin (2001) using the three Thomsen parameters: $\epsilon = 0.110$, $\delta = -0.035$, and $\eta = .155$. The gray line (green in color) superimposed onto the impulse response is the result of cutting the surface at zero subsurface offset, and thus corresponds to the conventional impulse response of prestack migration. The black line superimposed onto the impulse response is the result of cutting the surface at zero midpoint. In Figure 4 these two lines are superimposed onto the corresponding vertical sections cut from the images computed by an anisotropic wavefield source-receiver migration applied with the same parameters described above. Figure 4b shows the conventional migration impulse response, whereas Figure 4a shows the zero-midpoint section. The lines computed by applying the kinematic equations perfectly match the impulse responses computed using wavefield migration, confirming the accuracy of the kinematic equations.
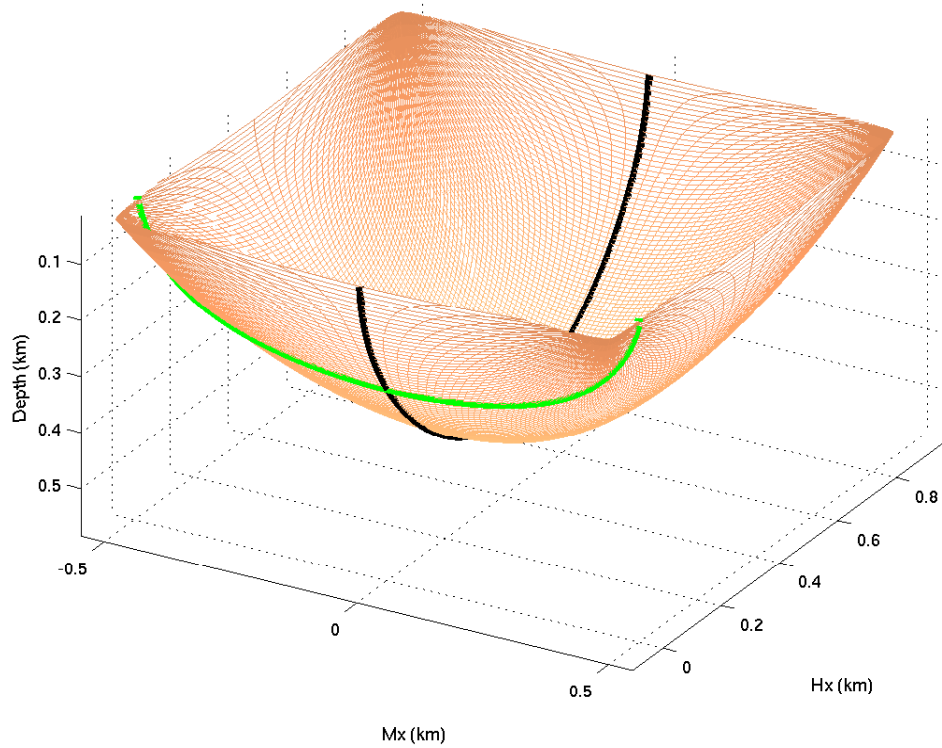
Figure 3: Impulse response of generalized anisotropic prestack migration. The gray line (green in color) superimposed onto the impulse response corresponds to the conventional impulse response of prestack migration. biondo1-surf_taylor_hxd_dot_4 [CR]

Figure 4: Vertical sections cut from the impulse response computed by an anisotropic wavefield source-receiver migration. The lines superimposed onto the images correspond to the lines superimposed onto the surface shown in Figure 3 and are computed by applying the kinematic expressions presented in equations 18–24. biondo1-Surf-taylor_hxd_.4-overn [CR]
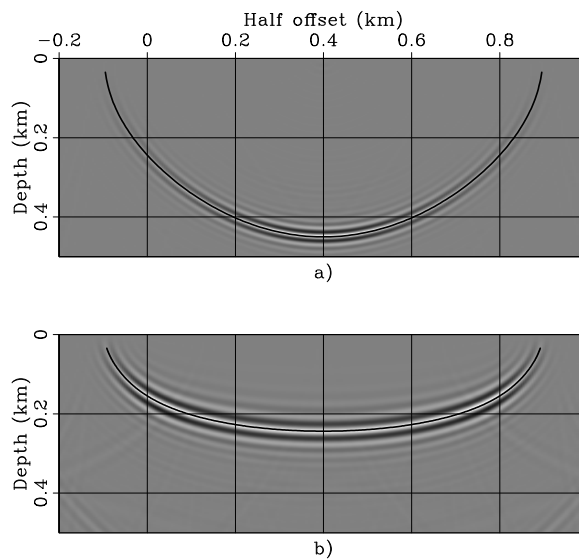
Analytical evaluation of the tangent plane to the impulse response

The expression for the generalized impulse response of prestack anisotropic migration leads to the analytical evaluation of the offset dip and midpoint dip along the planes tangent to the impulse response, as a function of the group angles and velocity. In this section I demonstrate that in the simple case of flat reflectors this analysis leads to exactly the same results as the phase-space analysis presented in the previous section. The derivation of the general relationships expressed in equations 13 and 12, which are valid for an arbitrary reflector's dip, is left to the reader.

By applying elementary analytical geometry, I demonstrate in Appendix B that the derivative of the depth with respect to the subsurface offset, at constant midpoint, is given by:

$$\left.\frac{\partial z_\xi}{\partial h_\xi}\right|_{m_\xi=\overline{m}_\xi} = -\frac{\frac{\partial z_\xi}{\partial \alpha_x}\frac{\partial m_\xi}{\partial \gamma} - \frac{\partial z_\xi}{\partial \gamma}\frac{\partial m_\xi}{\partial \alpha_x}}{\frac{\partial m_\xi}{\partial \alpha_x}\frac{\partial h_\xi}{\partial \gamma} - \frac{\partial m_\xi}{\partial \gamma}\frac{\partial h_\xi}{\partial \alpha_x}}, \tag{25}$$

and the derivative of the depth with respect to the midpoint, at constant subsurface offset, is given by:

$$\left.\frac{\partial z_\xi}{\partial m_\xi}\right|_{h_\xi=\overline{h}_\xi} = -\frac{\frac{\partial z_\xi}{\partial \alpha_x}\frac{\partial h_\xi}{\partial \gamma} - \frac{\partial z_\xi}{\partial \gamma}\frac{\partial h_\xi}{\partial \alpha_x}}{\frac{\partial m_\xi}{\partial \alpha_x}\frac{\partial h_\xi}{\partial \gamma} - \frac{\partial m_\xi}{\partial \gamma}\frac{\partial h_\xi}{\partial \alpha_x}}. \tag{26}$$

In the special case of flat reflectors the $\partial z_\xi/\partial \alpha_x$ and $\partial h_\xi/\partial \gamma$ vanish, and thus equation 25 simplifies into the following expression:

$$
\begin{aligned}
\left.\frac{\partial z_\xi}{\partial h_\xi}\right|_{(m_\xi=\overline{m}_\xi,\,\alpha_x=0)} &= \frac{\left(\left.\frac{\partial z_\xi}{\partial \gamma}\right|_{L=\overline{L}}+\frac{\partial L}{\partial \gamma}\cos\gamma\right)\frac{\partial m_\xi}{\partial \alpha_x}}{\left(\left.\frac{\partial h_\xi}{\partial \gamma}\right|_{L=\overline{L}}-\frac{\partial L}{\partial \gamma}\sin\gamma\right)\frac{\partial m_\xi}{\partial \alpha_x}} \\[2ex]
&= \frac{\left.\frac{\partial z_\xi}{\partial \gamma}\right|_{L=\overline{L}}+\frac{\partial L}{\partial \gamma}\cos\gamma}{\left.\frac{\partial h_\xi}{\partial \gamma}\right|_{L=\overline{L}}-\frac{\partial L}{\partial \gamma}\sin\gamma}.
\end{aligned} \tag{27}
$$

By substituting into equation 27 the appropriate derivative of the image coordinates and of the half path-length with respect to the angles, all provided in Appendix A, I further simplify the expression into the following:

$$\left.\frac{\partial z_\xi}{\partial h_\xi}\right|_{(m_\xi=\overline{m}_\xi,\,\alpha_x=0)} = \frac{\tan\gamma + \frac{1}{S}\frac{\partial S}{\partial \gamma}}{1 - \frac{1}{S}\frac{\partial S}{\partial \gamma}\tan\gamma}. \tag{28}$$

Finally, by applying the transformation from group angles into phase angles expressed in equation 4, I obtain the final result that for flat reflectors the subsurface-offset dip is exactly equal to the tangent of the phase aperture angle $\widetilde{\gamma}$; that is:

$$\left.\frac{\partial z_\xi}{\partial h_\xi}\right|_{(m_\xi=\overline{m}_\xi,\,\alpha_x=0)} = \tan\widetilde{\gamma}. \tag{29}$$

Numerical examples of aperture angle along impulse responses

The analytical kinematic results can be verified by numerical computations of impulse re-
sponses by wavefield migration and transformation of the resulting prestack image cubes into
the angle domain. Figure 5 shows four zero subsurface-offset sections cut through the impulse
responses computed by wavefield-continuation anisotropic migration for three anisotropic
rocks and for an isotropic rock. The first anisotropic rock is the Taylor Sand defined above.
The second is the Mesa Clay Shale as defined by Tsvankin (2001) using the three Thomsen
parameters: $\epsilon = 0.189$, $\delta = 0.204$, and $\eta = -.01$. The third is derived from the Green River
Shale as described by Tsvankin (2001) by halving the anisotropic parameters (ϵ and δ); that
is, it is defined by the three Thomsen parameters: $\epsilon = 0.0975$, $\delta = -0.11$, and $\eta = .266$. The
strong anelliptic nature of the original Green River Shale ($\eta = .74$) causes the group-slowness
approximation in equation 6 to break down, and makes the kinematic computations based on
ray tracing, and thus on group velocity and angles, inconsistent with wavefield migrations
based on the dispersion relation in equation 7. Hereupon I will refer to this rock, for obvious
reasons, as the GreenLight River Shale. Notice that the GreenLight River Shale is still strongly
elliptical.

The other parameters defining the impulse responses are the same as for Figure 3; that
is, $t_D = .9$ seconds, $m_D = 0$ kilometers, and $h_D = .4$ kilometers, and vertical slowness $S_V =$
1 s/km. Figure 5a shows the isotropic case, Figure 5b shows the Taylor Sand case, Figure 5c
shows the Mesa Clay Shale case, and Figure 5d shows the GreenLight River Shale case. As
in Figure 4, the line superimposed onto the images represent the impulse response computed
using the kinematic expressions in equations 18–24. The kinematic curves perfectly predict
the shape of the images even for very steep dips.

Figure 6 shows two-dimensional slices cut through the cube obtained by the transformation
to the angle domain of the impulse responses shown in Figure 5. The slices are cut at the
midpoint and depth corresponding to the expected location of the impulse responses; that is, at
the location tracked by the lines shown in Figure 5. There are three lines superimposed onto the
angle-domain images. The solid lines display the numerical computation of $\arctan(\partial z_\xi / \partial h_\xi)$
by applying equation 25. They perfectly track, as expected, the results of the transformation
of the prestack images to angle domain. The dotted lines display the phase aperture angle
$\widetilde{\gamma}$. As expected, they overlap with the solid line around the zero midpoint (i.e. flat reflector),
and depart from them at larger midpoints, which correspond to steeper reflections. However,
the error introduced by ignoring the difference between $\arctan(\partial z_\xi / \partial h_\xi)$ and $\widetilde{\gamma}$ is small, and
likely to be negligible in most practical situations. Finally, the dashed lines display the group
aperture angle γ. The differences between γ and $\widetilde{\gamma}$ are substantial, up to 20% in some cases.
Ignoring them might be detrimental to the application of ADCIGs. Notice that in the isotropic
case the three lines perfectly overlap and all of them match the image.
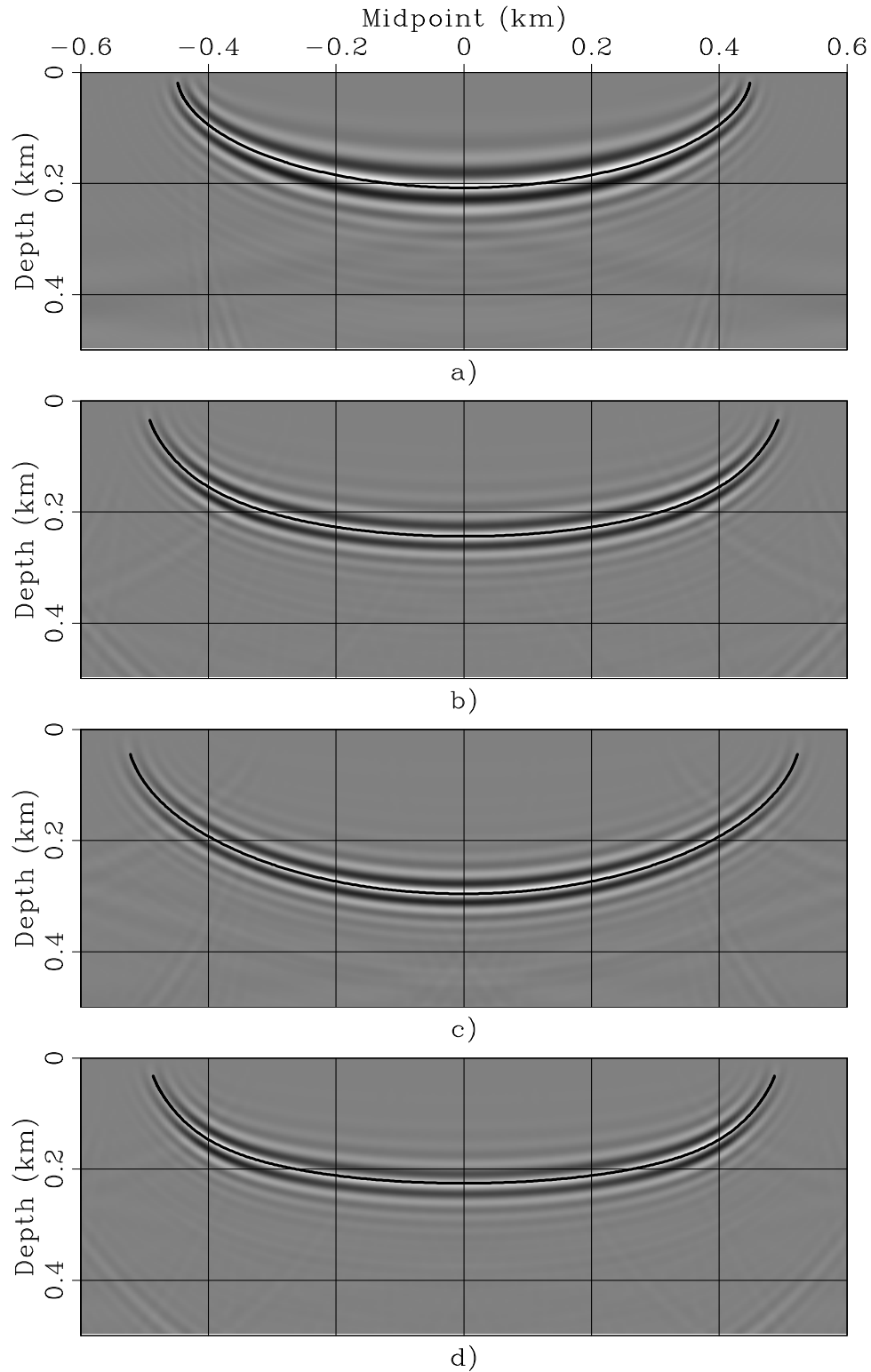
Figure 5: Impulse responses evaluated at zero subsurface offset for four rock types: a) Isotropic, b) Taylor Sand, c) Mesa Clay Shale, and d) GreenLight River Shale. Superimposed onto the images are the impulse responses computed by the kinematic expressions presented in equations 18–24.   biondo1-Quad_hxd_.4-overn   [CR]
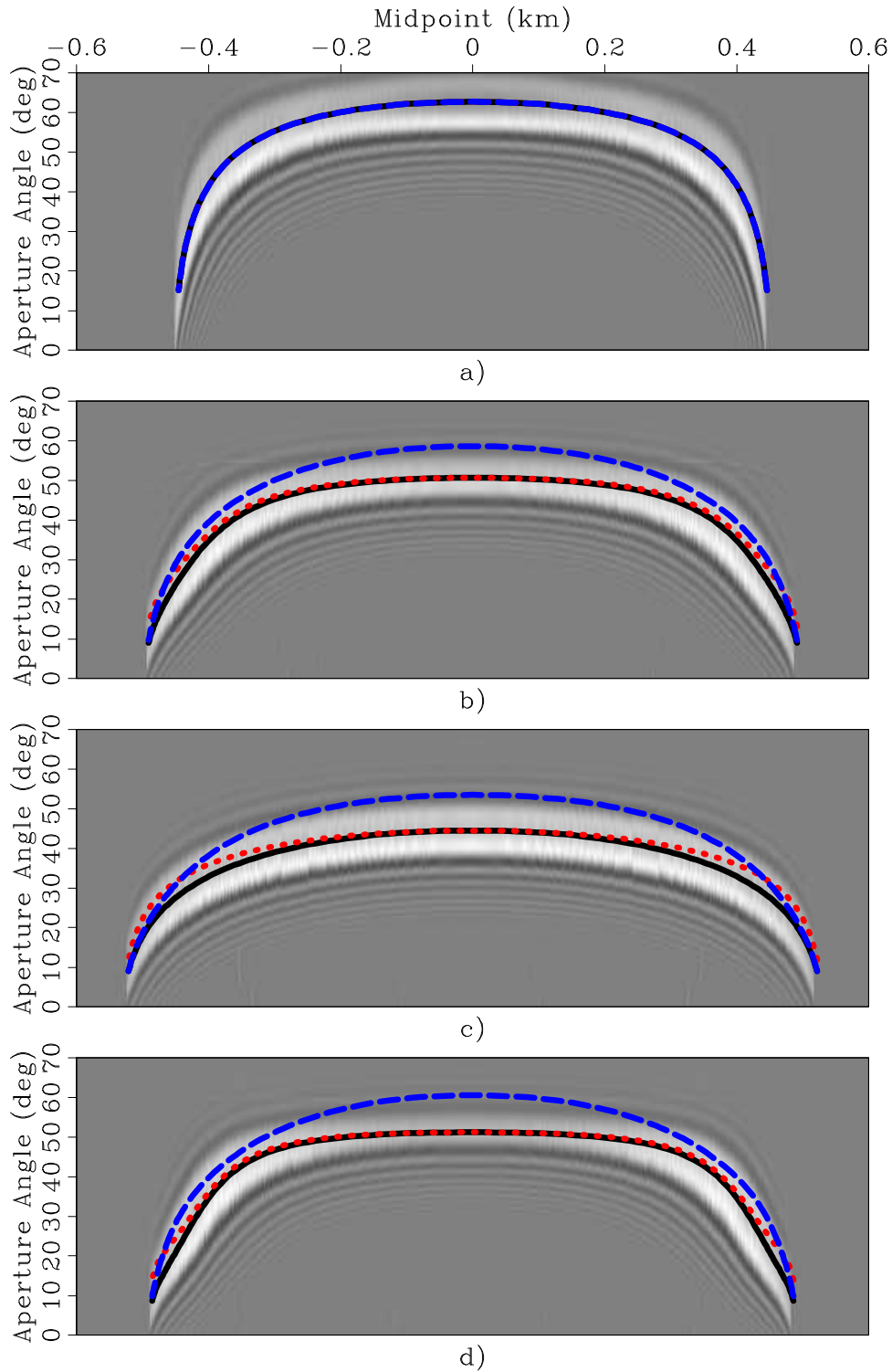
Figure 6: Slices of the impulse responses transformed into the angle-domain for four rock types: a) Isotropic, b) Taylor Sand, c) Mesa Clay Shale, and d) GreenLight River Shale. Superimposed onto the images there are the curves computed by applying the kinematic analysis: γ (dashed line), $\widetilde{\gamma}$ (dotted line), and $\arctan(\partial z_\xi / \partial h_\xi)$ (solid line).

biondo1-Quad_Mx-Ang_hxd_.4-overn [CR]

GULF OF MEXICO DATA EXAMPLE

To illustrate the proposed methodology for computing ADCIGs from prestack images obtained by anisotropic migration, I migrated a 2-D line extracted from a 3-D data set that was kindly provided to SEP by ExxonMobil. I chose the location of the 2-D line in an area where the sediments are mostly flat in the cross-line direction and where the salt flanks are mostly perpendicular to the in-line direction.

The data set was acquired in the Gulf of Mexico over an existing reservoir. Therefore several borehole seismic data sets were available in addition to the surface data to constraint the estimation of the anisotropic parameters. ExxonMobil provided SEP with three anisotropic-parameter cubes resulting from a joint inversion of the surface data and the borehole data (Krebs et al., 2003). Figure 7 shows the vertical slices cut through these cubes at the cross-line location corresponding to the 2-D line that I migrated. Panel a) displays the vertical velocity, panel b) displays the values of δ, and panel c) displays the values of η. To avoid artifacts caused by sharp parameter contrasts, for migration I removed the salt body from the functions displayed in Figure 7. I "infilled" the salt body with sediment-like values by interpolating the functions inward starting from the sediment values at the salt-sediment interface.

Figure 8 shows the result of anisotropic prestack depth migration. All the reflectors are nicely imaged, including the steep salt flank on the right-hand side of the salt body. The shallow tract of the salt flank on the left-hand side of the body is poorly imaged because it has large cross-line dip components. The two vertical lines superimposed onto the image identify the surface location of the ADCIGs displayed in Figure 9. The two black bars superimposed onto the image identify the reflections for which I analyzed the ADCIG in details. Figure 9 shows two ADCIGs computed by slant stacking the prestack image along the subsurface axis. Both CIGs show fairly flat moveout, indicating that the anisotropic velocity model used for migration is accurate, though not perfect. The shallow reflections show the most noticeable departure from flatness (they frown downward) because these reflectors were not the focus of the velocity model-building efforts. The CIGs are taken at the location indicated by the vertical black lines in Figure 8; the CIG shown in panel a) is taken at the surface location of 3,725 meters and the CIG shown in panel b) is taken at the surface location of 11,625 meters. Within these two CIGs, I selected for detailed analysis the reflections corresponding to the black bars superimposed onto the image because they represent two 'typical' cases where the accuracy of the estimation of the reflection-aperture angle might be important. The shallow black bar on the left identifies a flat reflector illuminated with a wide range of aperture angles, up to 60 degrees. The wide angular range is potentially useful for constraining the value of the anisotropic parameters in the sediments. The deep black bar on the right identifies one of the potential reservoir sands, and thus it is a potential target for Amplitude Versus Angle (AVA) analysis using ADCIGs.

The plots in Figure 10 show the differences between the true phase aperture angle computed by iteratively solving the system of equations 16 and 17 and the aperture angle estimated by slant stacks (solid line) and the group aperture angle (dashed line). The group angles are computed by applying equation 2. The plot in panel a) corresponds to the shallow black bar on the left. The reflector is flat and the velocity parameters at the reflector are:
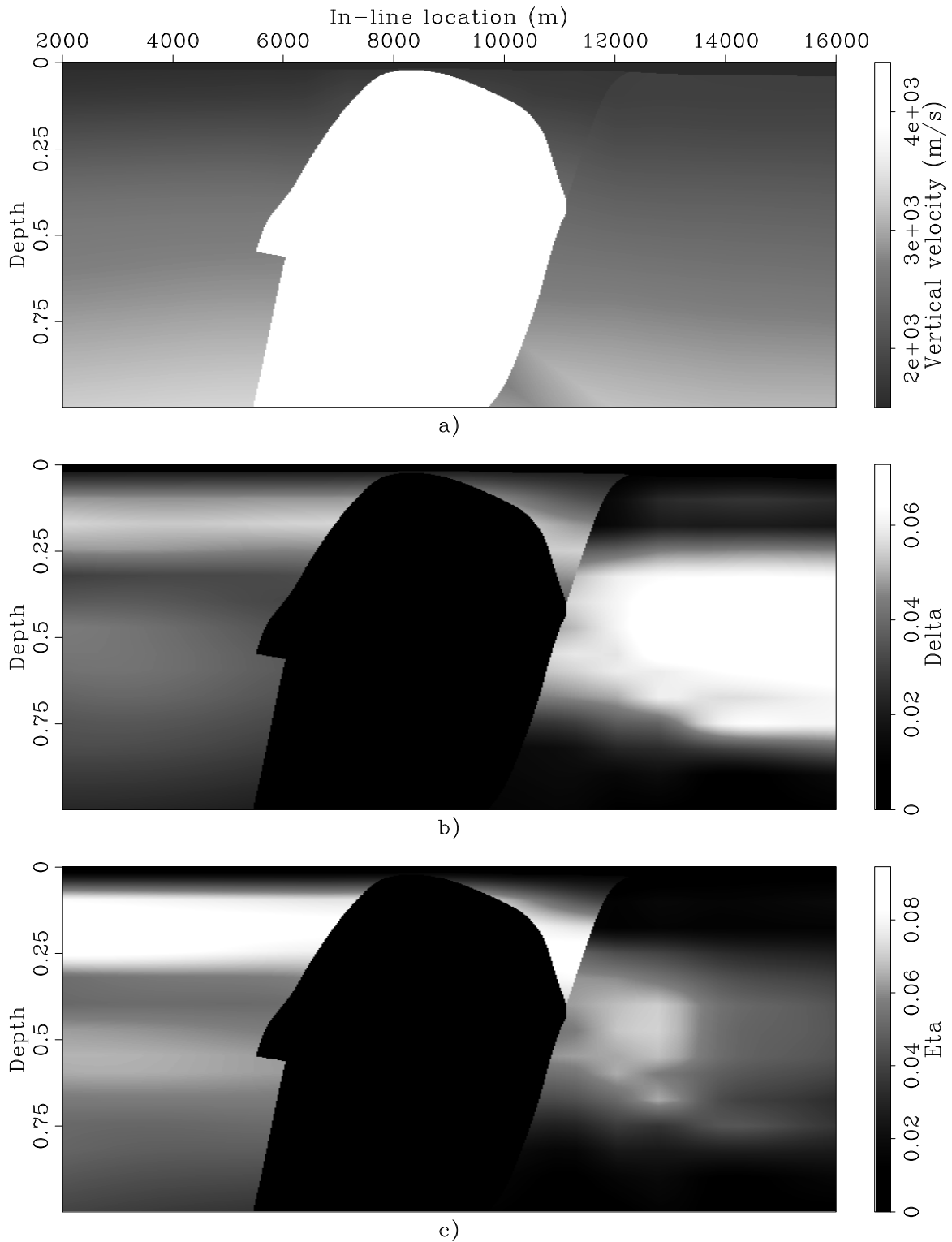
Figure 7: Vertical slices cut through the anisotropic velocity parameters cubes. Panel a) shows the vertical velocity field, panel b) shows the δ field, and panel c) shows the η field. I removed the salt body from the parameters functions used for migration, to avoid artifacts caused by sharp parameter discontinuities. biondo1-Par-Sections-overn [CR]

In-line location (m)
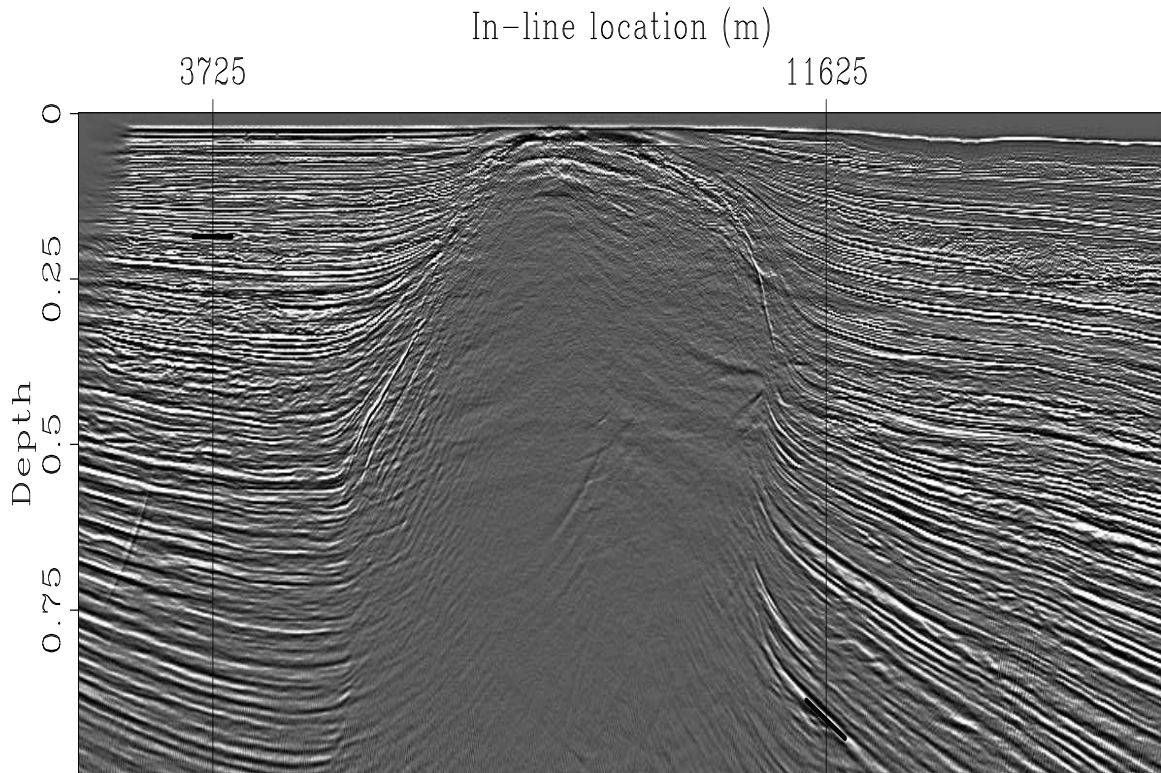
Figure 8: Image obtained by anisotropic prestack migration. The two vertical lines superimposed onto the image identify the surface location of the ADCIGs displayed in Figure 9. The two black bars superimposed onto the image identify the reflections analyzed in Figure 10. biondo1-Bar-Section-overn [CR]

$V_V = 1,995$ m/s, $\epsilon = 0.058$, $\delta = 0.0524$, and $\eta = .0905$. As expected, the aperture angles estimated by slant stack are exactly the same as the true ones because the reflector is flat. The maximum difference between the group aperture angle and the phase aperture angle is at 60 degrees, where the group angle is smaller by about 9 degrees than the phase angle; that is, about an error of about 15%.

The plot in panel b) corresponds the reservoir reflector (the deep black bar on the right). The dip of the reflector is about 25 degrees and the velocity parameters at the reflector are: $V_V = 3,060$ m/s, $\epsilon = 0.028$, $\delta = 0.0133$, and $\eta = .0144$. This area is weakly anisotropic (black in Figure 7b in Figure 7c) and thus the angular errors are small (≤ 1 degree) even if the reflector is dipping. Finally, the plot in panel c) corresponds to the hypothetical situation in which the reservoir was located in a more strongly anisotropic area than it actually is. To test the accuracy limits of approximating the phase aperture angles with the subsurface-offset slopes in the prestack image, I set the anisotropic parameters to be the highest value in the section; that is: ;$\epsilon = 0.172$, $\delta = 0.07$, and $\eta = .09$, and kept the vertical velocity and reflector's dip the same as in the previous case. The reflector is dipping and consequently the aperture angle estimated by slant stacks is lower than the true aperture angle. However, the error is small (≤ 2 degree) even at large aperture angle, and even smaller (≤ 1 degree) within

the angular range actually illuminated by the data ($0 \leq \widetilde{\gamma} \leq 30°$). Even in this "extreme" case the angular error is unlikely to have any significant negative effect on the accuracy of the AVA analysis of the reservoir reflection.

CONCLUSIONS

The methodology for computing and analyzing ADCIGs that has been recently developed for isotropic media can be generalized to prestack images computed using anisotropic prestack migration. This generalization opens the possibility of performing residual moveout velocity analysis and AVA analysis after anisotropic wavefield-continuation migration.

The transformation to angle domain performed by slant-stacking the prestack image along the subsurface-offset axis generates angle gathers that are approximately function of the phase aperture angle. When the accuracy of this approximation is not sufficient, the computation of the true aperture angles requires the measurement from the image of the geological dips of the reflections.

The differences between the true phase angle and the subsurface-offset slopes measured by slant stacks are caused by the difference in propagation velocity between the incident and the reflected waves. In a general TTI medium, the differences vanish for events normal to the isotropic axis of symmetry. In a VTI medium the differences vanish for flat reflectors and they are small unless the anisotropy is strong, the dips steep, and the aperture angle wide. This conclusion is supported by the detailed analysis of the ADCIGs generated my migrating a real data set in the presence of fairly strong anisotropy and steep salt flanks.

ACKNOWLEDGMENTS

REFERENCES

Bear, L., Dickens, T., and Traynin, P., 2003, Incorporating nonseismic information for improved imaging with anisotropic PSDM: 73rd Ann. Internat. Meeting, Soc. of Expl. Geophys., Expanded Abstracts, 949–952.

Biondi, B., and Sava, P., 1999, Wave-equation migration velocity analysis: 69th Ann. Internat. Meeting, Soc. of Expl. Geophys., Expanded Abstracts, 1723–1726.

Biondi, B., and Symes, W. W., 2003, Angle-domain common-image gathers for migration velocity analysis by wavefield-continuation imaging: Geophysics, **69**, 1283–1298.

Biondi, B., and Tisserant, T., 2004, 3-D angle-domain common-image gathers for migration velocity analysis: Geophisical Prospecting, **52**, 575–591.

Biondi, B., 2005, Residual moveout in anisotropic angle-domain common image gathers: SEP–**123**.

Clapp, R., and Biondi, B., 2000, Tau domain migration velocity analysis using angle CRP gathers and geologic constrains: 70th Ann. Internat. Meeting, Soc. of Expl. Geophys., Expanded Abstracts, 926–929.

Dellinger, J., and Muir, F., 1985, Two domains of anisotropy: SEP–**44**, 59–62.

Fomel, S., 2002, Applications of plane-wave destruction filters: Geophysics, **67**, 1946–1960.

Fowler, P., 2003, Practical VTI approximations: a systematic anatomy: Journal of Applied Geophysics, **69**, 347–367.

Krebs, J., Bear, L., and Liu, J., 2003, Integrated velocity model estimation for accurate imaging: 73rd Ann. Internat. Meeting, Soc. of Expl. Geophys., Expanded Abstracts, 2084–2087.

Prucha, M., Biondi, B., and Symes, W. W., 1999, Angle-domain common-image gathers by wave-equation migration: 69th Ann. Internat. Meeting, Soc. Expl. Geophys., Expanded Abstracts, 824–827.

Rickett, J., and Sava, P., 2002, Offset and angle-domain common image-point gathers for shot-profile migration: Geophysics, **67**, 883–889.

Rosales, D. A., and Biondi, B., 2005, Converted-mode angle-domain common-image gathers for migration velocity analysis: SEP–**120**, 283–296.

Rosales, D. A., and Rickett, J., 2001, PS-wave polarity reversal in angle domain common-image gathers: 71th Ann. Internat. Meeting, Soc. Expl. Geophys., Expanded Abstracts, 1843–1846.

Sarkar, D., and Tsvankin, I., 2004, Anisotropic migration velocity analysis: Application to a data set from West Africa: 74th Ann. Internat. Meeting, Soc. of Expl. Geophys., Expanded Abstracts, 2399–2402.

Sava, P., and Fomel, S., 2003, Angle-domain common-image gathers by wavefield continuation methods: Geophysics, **68**, 1065–1074.

Stolk, C. C., and Symes, W. W., 2003, Kinematic artifacts in prestack depth migration: Geophysics, **69**, 562–575.

Tsvankin, I., 2001, Seismic signatures and analysis of reflection data in anisotropic media: Elsevier Science.

Wang, J., Khuel, H., and Sacchi, M., 2005, High-resolution wave-equation ava imaging: Algorithm and tests with a data set from the western canadian sedimentary basin: Geophysics, **70**, S91—S99.

APPENDIX A

CONVERSION FROM AVERAGE ANGLES TO TRUE APERTURE ANGLES

In this appendix I present the expressions for evaluating the true reflection angles $\widetilde{\gamma}_s$ and $\widetilde{\gamma}_r$ for the incident and reflected plane waves, from the 'normalized slowness difference" $\Delta_{\widetilde{S}} = (\widetilde{S}_r - \widetilde{S}_s)/(\widetilde{S}_r + \widetilde{S}_s)$ and from the average aperture angles $\widetilde{\gamma}$ computed by solving equations 16 and 17.

Rosales and Biondi (2005) derived these relationships as follows:

$$\tan\widetilde{\gamma}_s \quad = \quad \frac{\frac{1+\Delta_{\widetilde{S}}}{1-\Delta_{\widetilde{S}}}\sin 2\widetilde{\gamma}}{1 + \frac{1+\Delta_{\widetilde{S}}}{1-\Delta_{\widetilde{S}}}\cos 2\widetilde{\gamma}} \tag{A-1}$$

$$\tan\widetilde{\gamma}_r \quad = \quad \frac{\sin 2\widetilde{\gamma}}{\frac{1+\Delta_{\widetilde{S}}}{1-\Delta_{\widetilde{S}}} + \cos 2\widetilde{\gamma}}. \tag{A-2}$$

It is easy to verify that when $\Delta_{\widetilde{S}} = 0$ (isotropic case) we get, as expected, $\widetilde{\gamma}_s = \widetilde{\gamma}_r = \widetilde{\gamma}_r$.

APPENDIX B

ANALYTICAL EVALUATION OF THE TANGENT PLANE TO THE IMPULSE RESPONSE

In this appendix I derive the expressions for evaluating the derivatives of image depth z_ξ with respect to the subsurface offset h_ξ and the midpoint m_ξ; these derivatives are computed along the tangent plane to the impulse response of the generalized migration operator, which is defined in equations 18–24.

I start by deriving the equation for the vector normal to the impulse-response surface, $\vec{n}$:

$$\vec{n} = \begin{vmatrix} \vec{z}_\xi & \vec{m}_\xi & \vec{h}_\xi \\ \frac{\partial z_\xi}{\partial \alpha_x} & \frac{\partial m_\xi}{\partial \alpha_x} & \frac{\partial h_\xi}{\partial \alpha_x} \\ \frac{\partial z_\xi}{\partial \gamma} & \frac{\partial m_\xi}{\partial \gamma} & \frac{\partial h_\xi}{\partial \gamma} \end{vmatrix}$$

$$= \left(\frac{\partial m_\xi}{\partial \alpha_x}\frac{\partial h_\xi}{\partial \gamma} - \frac{\partial m_\xi}{\partial \gamma}\frac{\partial h_\xi}{\partial \alpha_x} \right)\vec{z}_\xi + \left(-\frac{\partial z_\xi}{\partial \alpha_x}\frac{\partial h_\xi}{\partial \gamma} + \frac{\partial z_\xi}{\partial \gamma}\frac{\partial h_\xi}{\partial \alpha_x} \right)\vec{m}_\xi + \left(\frac{\partial z_\xi}{\partial \alpha_x}\frac{\partial m_\xi}{\partial \gamma} - \frac{\partial z_\xi}{\partial \gamma}\frac{\partial m_\xi}{\partial \gamma} \right)\vec{h}_\xi, \tag{B-1}$$

where $\vec{z}_\xi$, $\vec{m}_\xi$, and $\vec{h}_\xi$ are respectively the unit vectors along the three dimensions z_ξ, m_ξ, and h_ξ.

The equation of the tangent plane at the image point with coordinates $\left(\overline{z}_\xi, \overline{m}_\xi, \overline{h}_\xi \right)$ is given

by:

$$T\left(z_\xi, m_\xi, h_\xi\right) = \left(\frac{\partial m_\xi}{\partial \alpha_x}\frac{\partial h_\xi}{\partial \gamma} - \frac{\partial m_\xi}{\partial \gamma}\frac{\partial h_\xi}{\partial \alpha_x}\right)\left(z_\xi - \overline{z}_\xi\right)$$

$$+ \left(-\frac{\partial z_\xi}{\partial \alpha_x}\frac{\partial h_\xi}{\partial \gamma} + \frac{\partial z_\xi}{\partial \gamma}\frac{\partial h_\xi}{\partial \alpha_x}\right)\left(m_\xi - \overline{m}_\xi\right)$$

$$+ \left(\frac{\partial z_\xi}{\partial \alpha_x}\frac{\partial m_\xi}{\partial \gamma} - \frac{\partial z_\xi}{\partial \gamma}\frac{\partial m_\xi}{\partial \alpha_x}\right)\left(h_\xi - \overline{h}_\xi\right) = 0. \tag{B-2}$$

The derivative of the depth with respect o the subsurface offset, at constant midpoint, is given by:

$$\left.\frac{\partial z_\xi}{\partial h_\xi}\right|_{m_\xi = \overline{m}_\xi} = -\frac{\left.\frac{\partial T}{\partial h_\xi}\right|_{m_\xi = \overline{m}_\xi}}{\left.\frac{\partial T}{\partial z_\xi}\right|_{m_\xi = \overline{m}_\xi}} = -\frac{\frac{\partial z_\xi}{\partial \alpha_x}\frac{\partial m_\xi}{\partial \gamma} - \frac{\partial z_\xi}{\partial \gamma}\frac{\partial m_\xi}{\partial \alpha_x}}{\frac{\partial m_\xi}{\partial \alpha_x}\frac{\partial h_\xi}{\partial \gamma} - \frac{\partial m_\xi}{\partial \gamma}\frac{\partial h_\xi}{\partial \alpha_x}}. \tag{B-3}$$

and similarly the derivative of the depth with respect to the midpoint, at constant subsurface offset, is given by:

$$\left.\frac{\partial z_\xi}{\partial m_\xi}\right|_{h_\xi = \overline{h}_\xi} = -\frac{\left.\frac{\partial T}{\partial m_\xi}\right|_{h_\xi = \overline{h}_\xi}}{\left.\frac{\partial T}{\partial z_\xi}\right|_{h_\xi = \overline{h}_\xi}} = -\frac{\frac{\partial z_\xi}{\partial \alpha_x}\frac{\partial h_\xi}{\partial \gamma} - \frac{\partial z_\xi}{\partial \gamma}\frac{\partial h_\xi}{\partial \alpha_x}}{\frac{\partial m_\xi}{\partial \alpha_x}\frac{\partial h_\xi}{\partial \gamma} - \frac{\partial m_\xi}{\partial \gamma}\frac{\partial h_\xi}{\partial \alpha_x}}. \tag{B-4}$$

To evaluate equations B-3–B-4. we need to evaluate the following partial derivatives, obtained by differentiating the expressions in equations 18–20:

$$\frac{\partial z_\xi}{\partial \alpha_x} = -L\left(\alpha_x, \gamma\right)\frac{\tan\alpha_x}{\cos\alpha_x \cos\gamma}\left(\cos^2\alpha_x + \sin^2\gamma\right) + \frac{\partial L\left(\alpha_x, \gamma\right)}{\partial \alpha_x}\frac{\cos^2\alpha_x - \sin^2\gamma}{\cos\alpha_x \cos\gamma},$$

$$\frac{\partial z_\xi}{\partial \gamma} = -L\left(\alpha_x, \gamma\right)\frac{\tan\gamma}{\cos\alpha_x \cos\gamma}\left(\cos^2\gamma + \sin^2\alpha_x\right) + \frac{\partial L\left(\alpha_x, \gamma\right)}{\partial \gamma}\frac{\cos^2\alpha_x - \sin^2\gamma}{\cos\alpha_x \cos\gamma},$$

$$\frac{\partial m_\xi}{\partial \alpha_x} = -L\left(\alpha_x, \gamma\right)\frac{\cos\alpha_x}{\cos\gamma} - \frac{\partial L\left(\alpha_x, \gamma\right)}{\partial \alpha_x}\frac{\sin\alpha_x}{\cos\gamma},$$

$$\frac{\partial m_\xi}{\partial \gamma} = -L\left(\alpha_x, \gamma\right)\frac{\sin\gamma \sin\alpha_x}{\cos^2\gamma} - \frac{\partial L\left(\alpha_x, \gamma\right)}{\partial \gamma}\frac{\sin\alpha_x}{\cos\gamma},$$

$$\frac{\partial h_\xi}{\partial \alpha_x} = -L\left(\alpha_x, \gamma\right)\frac{\sin\gamma \sin\alpha_x}{\cos^2\alpha_x} - \frac{\partial L\left(\alpha_x, \gamma\right)}{\partial \alpha_x}\frac{\sin\gamma}{\cos\alpha_x},$$

$$\frac{\partial h_\xi}{\partial \gamma} = -L\left(\alpha_x, \gamma\right)\frac{\cos\gamma}{\cos\alpha_x} - \frac{\partial L\left(\alpha_x, \gamma\right)}{\partial \gamma}\frac{\sin\gamma}{\cos\alpha_x}. \tag{B-5}$$

The derivative of path length are evaluated as follows:

$$\frac{\partial L}{\partial \alpha_x} = \frac{-t_D}{\left[(S_r + S_s) + (S_r - S_s)\tan\alpha_x \tan\gamma\right]^2}$$

$$\left[\left(\frac{\partial S_r}{\partial \alpha_x} + \frac{\partial S_s}{\partial \alpha_x}\right) + \left(\frac{\partial S_r}{\partial \alpha_x} - \frac{\partial S_s}{\partial \alpha_x}\right)\tan\alpha_x \tan\gamma + \frac{(S_r - S_s)\tan\gamma}{\cos^2\alpha_x}\right], \tag{B-6}$$

and

$$\frac{\partial L}{\partial \gamma} = \frac{-t_D}{\left[(S_r + S_s) + (S_r - S_s)\tan\alpha_x \tan\gamma\right]^2}$$
$$\left[\left(\frac{\partial S_r}{\partial \gamma} + \frac{\partial S_s}{\partial \gamma}\right) + \left(\frac{\partial S_r}{\partial \gamma} - \frac{\partial S_s}{\partial \gamma}\right)\tan\alpha_x \tan\gamma + \frac{(S_r - S_s)\tan\alpha_x}{\cos^2\gamma}\right]. \qquad \text{(B-7)}$$

Application to the isotropic case

The application to the isotropic case is simpler than the anisotropic case because the derivative of the path length is zero, but it is instructive since it verifies known results through a completely different derivation. Substituting equations B-5 into equation B-3, I obtain:

$$\begin{aligned}
\left.\frac{\partial z_\xi}{\partial h_\xi}\right|_{m_\xi = \bar{m}_\xi} &= -\frac{L^2 \tan\gamma \left[\frac{\tan^2\alpha_x}{\cos^2\gamma}\left(\cos^2\alpha_x + \sin^2\gamma\right) - \frac{1}{\cos^2\gamma}\left(\cos^2\gamma + \sin^2\alpha_x\right)\right]}{L^2\left[1 - \tan^2\alpha_x \tan^2\gamma\right]} \\
&= -\frac{L^2 \tan\gamma \left[-1 + \sin^2\alpha_x \left(\frac{1}{\cos^2\gamma} - \frac{1}{\cos^2\gamma}\right) + \tan^2\alpha_x \tan^2\gamma\right]}{L^2\left[1 - \tan^2\alpha_x \tan^2\gamma\right]} \\
&= \tan\gamma, \qquad\qquad\qquad\qquad\qquad\qquad\qquad\qquad\qquad\qquad \text{(B-8)}
\end{aligned}$$

which shows that $\partial z_\xi / \partial h_\xi$ is independent from the dip angle α_x. This expression is consistent with the 2-D analysis by Sava and Fomel (2003) and the 3-D analysis by by Biondi and Tisserant (2004).

Figure 9: ADCIGs computed from the prestack image by slant stacking along the subsurface offset axis. The CIG shown in panel a) is taken at the surface location of 3,725 meters, and the CIG shown in panel b) is taken at the surface location of 11,625 meters. biondo1-Duo-aniso-overn [CR]
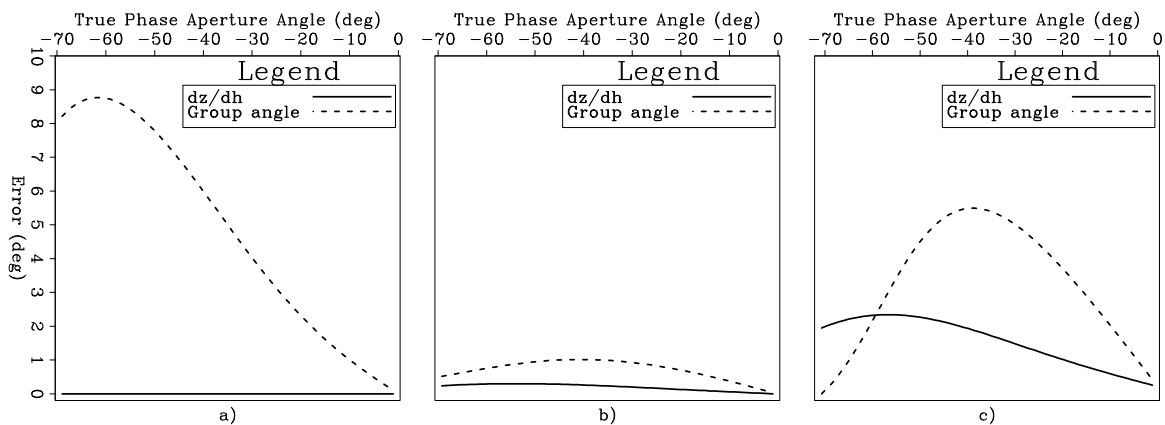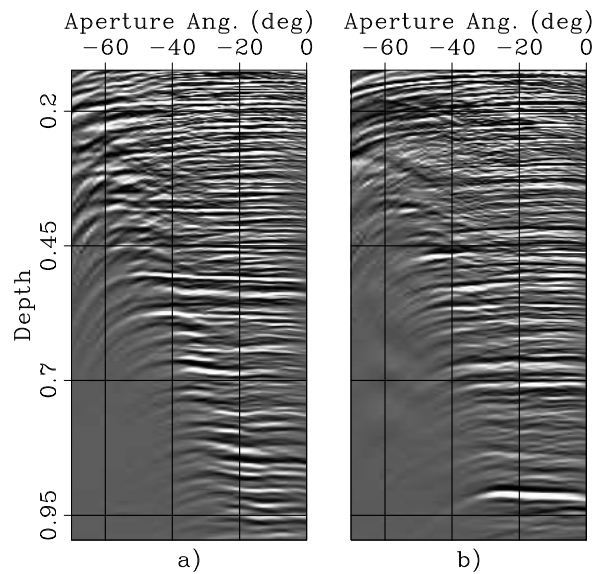
Figure 10: Differences between the true phase aperture angle and the aperture angle estimated by slant stacks (solid line) and the group aperture angle (dashed line). The plot in panel a) corresponds to the reflection identified with the shallow black bar on the left in Figure 8. The plot in panel b) corresponds the reservoir reflector (the deep black bar on the right). The plot in panel c) corresponds to the hypothetical situation in which the reservoir reflector was located in a more strongly anisotropic area than it actually is. biondo1-Trio-Ang-overn [CR]